ELSEVIER

Contents lists available at ScienceDirect

Sensors and Actuators Reports

journal homepage: www.sciencedirect.com/journal/sensors-and-actuators-reports





Enhancing room-temperature gas sensing performance of metal oxide semiconductor chemiresistors through 400 nm UV photoexcitation

Suporna Paul^a, Emily Resendiz Mendoza^a, Dung Thi Hanh To^a, Thomas F. Stahovich^b, Jennifer Schaefer^a, Nosang V. Myung^{a,*}

- ^a Chemical and Biomolecular Engineering, University of Notre Dame, Notre Dame, IN, 46556, USA
- b Department of Mechanical Engineering, University of California, Riverside, 92521, California, USA

ARTICLE INFO

Keywords: Chemiresistive MOS Semiconductors UV photoexcitation Toxic industrial chemicals

ABSTRACT

One of the most significant drawbacks of metal oxide (MOS) based chemiresistive gas sensors is the requirement of high operating temperature (250–450 °C), which results in significant power consumption and shorter lifetime. To develop room temperature (21 \pm 2 °C) MOS chemiresistive gas sensors, the sensing performance of different MOS nanostructures (i.e., tin (IV) oxide (SnO₂) nanoparticles (NPs), indium (III) oxide (In₂O₃) NPs, zinc oxide (ZnO) NPs, tungsten trioxide (WO₃) NPs, copper oxide (CuO) nanotubes (NTs), and indium tin oxide (In₉oSn₁₀O₃ (ITO)) NPs) were systematically investigated toward different toxic industrial chemicals (TICs) (i.e., nitrogen dioxide (NO₂), ammonia (NH₃), hydrogen sulfide (H₂S), carbon monoxide (CO), sulfur dioxide (SO₂) and volatile organic compounds (VOCs) (i.e., acetone (C₃H₆O), toluene (C₆H₅CH₃), ethylbenzene (C₆H₅CH₂CH₃), and p-xylene (C₆H₄(CH₃)₂)) in the presence and absence of 400 nm UV light illumination.

Sensing performance enhancement through photoexcitation is strongly dependent on the target analytes. Under 400 nm UV photoexcitation at 76.0 mW/cm² intensity, room temperature (21 \pm 2 °C) NO₂ sensing was readily achieved where SnO₂ NPs exhibited the highest sensor response (S=474.4 toward 10 ppm_m (parts per million by mass)) with good recovery followed by ZnO NPs > In₂O₃ NPs > ITO NPs. Meanwhile, indirect bandgap n-type WO₃ NPs showed limited NO₂ sensing performance under illumination, whereas p-type CuO NTs showed relatively good sensing response. The most significant improvements in SnO₂ compared to other MOS nanoparticles might be attributed to the highest number of photogeneration electrons, which rapidly reacted with adsorbed NO₂ species to enhance the reaction kinetics. WO₃ NPs showed a unique sensing response toward aromatic compounds (e.g., ethylbenzene and p-xylene) under UV illumination, where maximum sensitivity was achieved under 36 mW/cm² irradiation. Changing light intensity from 0.0 to 36.4 mW/cm², WO₃ showed 15.4-fold and 6.3-fold enhancement in sensing response toward 25 ppm_m ethylbenzene and 100 ppm_m p-xylene, respectively. 400 nm optical excitation has a limited effect on the sensing performance toward CO, SO₂, toluene, and acetone.

1. Introduction

Environmental pollution has become a severe problem due to the rise of industrial activity, urbanization, the release of exhaust fumes from vehicles, burning fossil fuels, and wildfires [1–3]. Therefore, air quality monitoring has become an essential part of our daily life to increase awareness of the presence of hazardous gases such as NO₂, NH₃, H₂S, CO, SO₂, and volatile organic compounds (VOCs) (i.e., toluene, acetone, xylene, and ethylbenzene). All these hazardous chemicals can cause severe health problems in humans, animals, and the ecosystem [4]. For

example, NO₂ is suspected to cause acid rain, ozone formation at ground level, and hazy air, all of which are harmful to the ecosystem and humans [5]. Additionally, it is assessed that breathing at higher levels of NO₂ may cause damage to the respiratory tract [5]. Furthermore, CO poisoning may lead to permanent heart damage, brain damage, and death [6]. Similarly, H₂S exposure at low levels may cause eye, nose, and throat irritation; exposure to high-level H₂S (100 ppm_m) holds the possibility of causing fatal toxicity [7,8]. Additionally, inhalation of toxic aromatic VOCs can lead to critical damage to the central nervous system and may cause cancer and mutagenesis [9].

E-mail address: nmyung@nd.edu (N.V. Myung).

^{*} Corresponding author

Various MOS (i.e., n-type: ferric oxide (Fe₂O₃) titanium dioxide (TiO₂), WO₃, ZnO, and SnO₂ [10,11], p-type MOS: CuO, nickel oxide (NiO), cobalt(II, III) oxide (Co₃O₄), and chromium(III) oxide (Cr₂O₃) [12,13]) nanostructures have been applied as chemiresistive gas sensing materials because of high sensitivity [10,14,15], fast response times [16], rapid recovery rates [14], high repeatability [13], wide range of analytes detection within varied chemical functional groups [15], and low-cost [12]. However, the requirement of elevated operating temperature [14,17] resulted in high power consumption [18-20] and limited the lifetime. Room temperature gas sensors that can detect various analytes with high sensing performance will be a game changer, especially devices with limited power sources (i.e., wearable devices). Unfortunately, lower electron density at the MOS conduction band at room temperature could result in lower sensing performance, affecting its utilization in practical applications [21]. Several research works included UV photoexcitation to demonstrate low-temperature (<100 °C) analyte detection through porous ZnO thin films (1 ppm_m NO₂ detection at 25 °C) [22], SnO₂ nanowires (100 ppb_m (parts per billion by mass)NO₂ detection at 25 °C) [23], mesoporous In₂O₃ (5 ppm_m NO₂ detection at room temperature) [24], In₂O₃ (2 ppm_m NO detection at 25 °C) [25], SnO₂ thin films (1ppm_m NO₂ detection at 20 °C) [26], ZnO microspheres (10 ppm_m ethanol detection at 25 °C) [27], etc.

Here, various MOS nanostructures (SnO2, In2O3, ZnO, WO3, CuO, and ITO) based chemiresistive gas sensors were fabricated and exposed to multiple target analytes to understand the effect of light illumination toward analyte detection at room temperature. In short, SnO2, In2O3, ZnO, and WO₃ are n-type semiconductors where the majority of charge carriers are electrons. Among these MOS materials, SnO2, In2O3, and ZnO are direct band gap materials, and WO3 is an indirect band gap semiconductor. The band is defined as the energy difference between the valence band's top and the conduction band's bottom. In a direct band gap semiconductor, the valence band's highest energy level aligns with the conduction band's lowest level at a similar momentum value. As a result, under light excitation, electrons could be excited and travel directly from the valence band to the conduction band without changing their momentum. However, in an indirect band gap semiconductor, the valence band's highest energy level and the conduction band's lowest energy level occur at a different momentum value.

In detail, SnO₂ has a wide direct band gap of 3.6 eV [28]. Due to its superior optical and electrical properties, it has been employed in applications such as solar cells, gas sensors, catalytic support materials, and light-emitting-diodes [29,30]. Additionally, In_2O_3 has a direct band gap of 3.6 eV and has been used in catalysis, solar cells, energy storage, and gas sensing [31]. Another wide band gap material is ZnO, with a direct band gap of 3.37 eV [32], binding energy of 60 meV, and high electron mobility (~200 cm²/Vs) [33,34]. In addition, ZnO is biocompatible, cost-effective, and thermally stable, enabling its application in a wide range of applications, such as photovoltaic devices, gas sensors, solar cells, and light-emitting diodes [35,36]. WO₃ has an indirect band gap of \sim 2.6–3.0 eV. Due to its non-toxic, chemical, thermal stability, and cost-effective nature, it has applications in photocatalysis and gas sensors [37,38]. CuO is an indirect band gap p-type semiconductor with a band gap of 1.2–1.9 eV in bulk materials [39], and the majority charge carrier is holes. It is also non-poisonous, cost-effective, and abundant in nature [39]. Moreover, ITO is a well-known n-type degenerate semiconductor [40,41]. ITO is composed of In₂O₃ and SnO₂ with a variation in mass or weight percentage ratio. It is called a degenerate semiconductor due to the high level of Sn doping. The carrier concentration of ITO depends on Sn doping and can also improve by increasing oxygen vacancies [42]. The energy band gap of ITO ranges from 3.5 to 4.3 eV [43]. ITO possessed a weight percentage (wt.%) ratio of In₂O₃:SnO₂ of 90:10 in this study.

In this work, six different MOS sensing materials (SnO_2 , In_2O_3 , ZnO, WO_3 , CuO, and ITO) were investigated toward eight different toxic industrial chemicals under 400 nm UV light illumination intensities from 0 (dark) to 76.0 mW/cm² at room temperature (21 ± 2 °C). Each analyte

was exposed at a broad concentration range to comprehensively study the gas sensing performance of the MOS chemiresistive sensors. The effect of UV light exposure on the sensitivity of the MOS materials was discussed. The novelty of this work is to advance the research field of room temperature gas sensor arrays by fabricating chemiresistive gas sensors with low energy consumption and using inexpensive commercially available MOS materials as the sensing materials. Additionally, this work indicates that the gas sensor arrays are highly sensitive toward various toxic gases under UV light exposure and demonstrate faster response-recovery times at ambient operating temperature (21 $\pm 2\,^{\circ}\text{C}$).

2. Experimental section

The experimental sections are divided into four sub-sections. Sub-Sections 2.1 and 2.2 provide detailed descriptions of the sensing materials solution preparation and sensing material characterization techniques, respectively. Sub-Sections 2.3 and 2.4 consecutively describe the high throughput testing systems and sensing property measurement details.

2.1. Sensing materials solution preparation

All chemicals and MOS nanomaterials were used without any further purification. The sensing material solvent was prepared by mixing N, Ndimethylformamide (DMF, ACS reagent, Fisher Scientific), and nanopure deionized water (resistivity of 18.17 M Ω .cm at 20 °C) in 50:50 volume% (vol. %) ratio. 10 mg of sensing materials (i.e., SnO2 nanoparticles (NPs) (99.9 % purity, the average primary particle size of 15.2 \pm 7.0 nm, Skyspring Nanomaterials Inc., USA), In₂O₃ NPs (99.999 %purity 5 N Powder, the average primary particle size of 44.7 \pm 14.5 nm, MSE Supplies, USA), ZnO NPs (99.8 % purity, the average primary NP size of 17.6 \pm 8.0 nm, AliExpress, China), WO₃ NPs (99.5 % purity, the average primary particle size of 88.1 \pm 42.9 nm, ROC/RIC Corp., USA), CuO nanotubes (NTs) (The average diameter of 8.8 \pm 1.8 nm, length =75-100 nm, Sigma Aldrich, USA) and ITO NPs (Particle size 20-70 nm, 99.99 % purity, MSE Supplies, USA)) were dispersed in 1 ml of DMF/ H₂O solvent and sonicated to form colloidal sensing material solutions at room temperature.

2.2. Material characterization

The morphology, lattice spacing, and compositional analysis were performed using high-resolution transmission electron microscopy (HRTEM, Spectra 30–300 (S)TEM). The phase structure and crystallinity of the materials were investigated using powder X-ray diffraction (XRD, Bruker D8 Advance, Cu-K α radiation, λ =1.5405 Å). XRD data were collected at a 0.01-degree increment from 5 to 80°. The average grain size was calculated by taking the full width at half maximum (FWHM-20) of the reflection plane and applying the Scherrer formula (Eq. (1)),

$$D = 0.9\lambda/\beta\cos\theta\tag{1}$$

where D= crystallite size, $\lambda=$ incident X-ray wavelength, CuK_{α} radiation, $\beta=$ FWHM in radians, and θ is the diffraction angle of the corresponding peak. Additionally, the UV–vis reflectance spectra were measured using a UV–Vis-NIR spectrophotometer (Ocean Optics, USA) for energy band gap calculation. A 6-channel LED light was included in the custom-made sensing chamber to investigate the optoelectrical property and effect of optical exposure on gas sensing performance.

2.3. Sensor fabrication and testing

Gas sensors were fabricated similar to the previously reported method [44]. In short, sensing materials were drop-casted on an individually addressable 60 sensors array (Fig. 1b). Custom-designed sensor system which consisted of 1) light illumination sub-system with

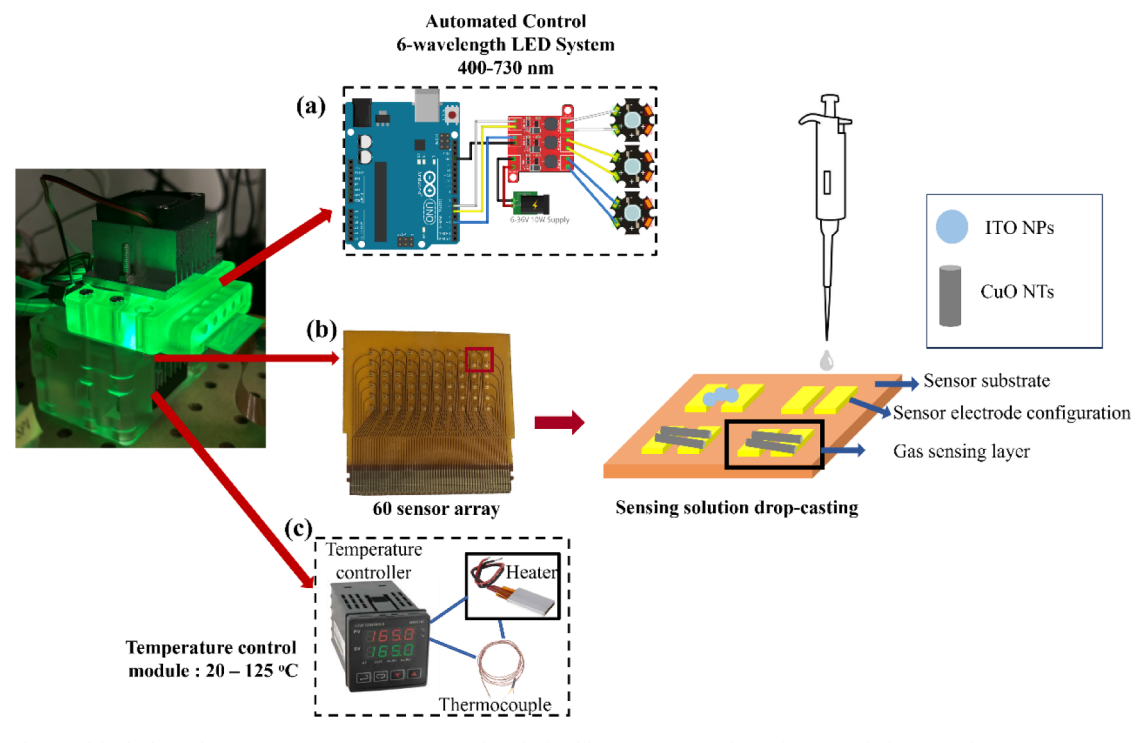


Fig. 1. Custom-designed high-throughput 60 sensors system consisted with flexible sensor array (b) with precise light (a) cnd temperature (c) controller. Drop-casting technique was used to fabricate sensor.

controllable light wavelength (i.e., 400 to 730 nm) and intensity (up to 76 mW/cm²), as shown in Fig. 1a, 2) temperature control sub-system (20 to 125 $^{\circ}$ C), as shown in Fig. 1c, 3) flow chamber, 4) electronic boards were used to measure the sensing response, and 5) LabVIEW controlled vapor generation to expose target analytes with known concentration to the gas sensor.

2.4. Electrical and sensing properties measurement conditions

Transient photoresponse and gas sensing experiments were conducted at room temperature (21±2 °C). Photocurrent response (R_p) was defined as $R_p = (R_0/R_L)$, where R_0 is the sensor's electrical baseline resistance under dark, and R_L is the sensor's resistance under light illumination. Photo-response time (T_{p90}) and recovery time (t_{p70}) were defined as the time required for the sensor to reach 90 % of the maximum change in resistance under light exposure and the time needed for the sensor to recover back to the 70 % baseline resistance under dark, respectively.

The sensor response was defined as $S=R_g/R_a$ for reducing and oxidizing analytes, where R_g is the sensor's electrical resistance when exposed to the analyte, and R_a is the electrical baseline resistance of the sensor in the carrier gas (i.e., dry air). Sensor response time (T_{s90}) and recovery time (T_{s90}) were defined as the time required for the sensor to reach 90 % of the maximum change in resistance under analyte exposure and the time needed for the sensor to recover back to the 70 % baseline resistance under air. If the baseline drift during the test, response and recovery time were calculated using local resistance values before and after analyte exposure at a specific concentration.

3. Results and discussion

3.1. Material properties

XRD analysis was conducted to study the crystalline and phase structure of the MOS nanostructure, as shown in Fig. 2. For SnO_2 NPs, a tetragonal rutile structure is observed (JCPDS Card No. 06–0416) [45]

with the average grain size of \sim 14.8 nm (Fig. 2a). $\rm In_2O_3$ NPs has a cubic phase (JCPDS Card No. 06–0416) [46] with the average grain size of \sim 24.5 nm (Fig. 2b). ZnO NP has a hexagonal structure (JCPDS Card No. 89–0510) [47] with the average grain size of \sim 17.2 nm (Fig. 2c). Both WO₃ NPs and CuO NTs have a monoclinic structure with the average grain size of \sim 39.1 nm and \sim 9.6 nm, respectively (Fig. 2d and e). ITO NPs consist of a 90:10 wt.% ratio between In: Sn where the XRD pattern matches with $\rm In_2O_3$ (JCPDS Card No. 06–0416) with the average grain size of \sim 18.4 nm [46] (Fig. 2f). Overall, no other characteristic peaks from impurities are detected confirming that the materials were pure.

Additionally, MOS morphology and lattice spacing were investigated using HRTEM. Typical HRTEM images of SnO₂ NPs, In₂O₃ NPs, ZnO NPs, WO₃ NPs, CuO NTs, and ITO NPs nanomaterials are shown in Figs. 3–5. SnO₂ NPs consist of aggregated particles with cubic morphology with an average nanoparticle size of 15.2 \pm 7.0 nm (Fig. 3a). The average SnO₂ particle size is similar to the average grain size, which might indicate that individual SnO₂ NP is a single crystal. Higher magnification analysis (Fig. 3b) shows the lattice planar spacing of \sim 3.42 Å (Fig. 3c) and \sim 2.71 Å (Fig. 3d), corresponding to the (110) and (101) planes of rutile SnO₂ structure. Similarly, the average nanoparticle size for In₂O₃ NPs shows less facets with an average NP size of 44.7 \pm 14.5 nm, which might indicate that NPs are polycrystal (Fig. 3e). The calculated lattice planar spacing are ~4.28 Å (Fig. 3g) and ~2.31 Å (Fig. 3h), corresponding to the (211) and (411) planes of cubic In₂O₃ structure. ZnO NPs show irregular shape with an average NPs size of 17.6 \pm 8.0 nm (Fig. 4a). An interplanar distance of ~ 2.59 Å (Fig. 4c), ~ 1.73 Å (Fig. 4c), and ~ 2.92 Å (Fig. 4d) are observed, which corresponds to the (002), (103), and (100) planes to the hexagonal ZnO structure, respectively.

 WO_3 NPs are much larger in particle size than other MOS NPs with an average particle size of 88.1 ± 42.9 nm (Fig. 4e). The lattice planar spacing are $\sim\!3.92$ Å, $\sim\!3.76$ Å, and $\sim\!2.70$ Å, which corresponds to the (002), (020), and (022) planes of the monoclinic WO_3 structure (Fig. 4g). CuO NTs show nanorod morphology (Fig. 5a) with an average diameter of 8.8 ± 1.8 nm. The length varies significantly from 8.0 to 110.0 nm. The clear lattice planner spacing is calculated to be 2.41 Å, corresponding to the (111) plane to the monoclinic CuO structure

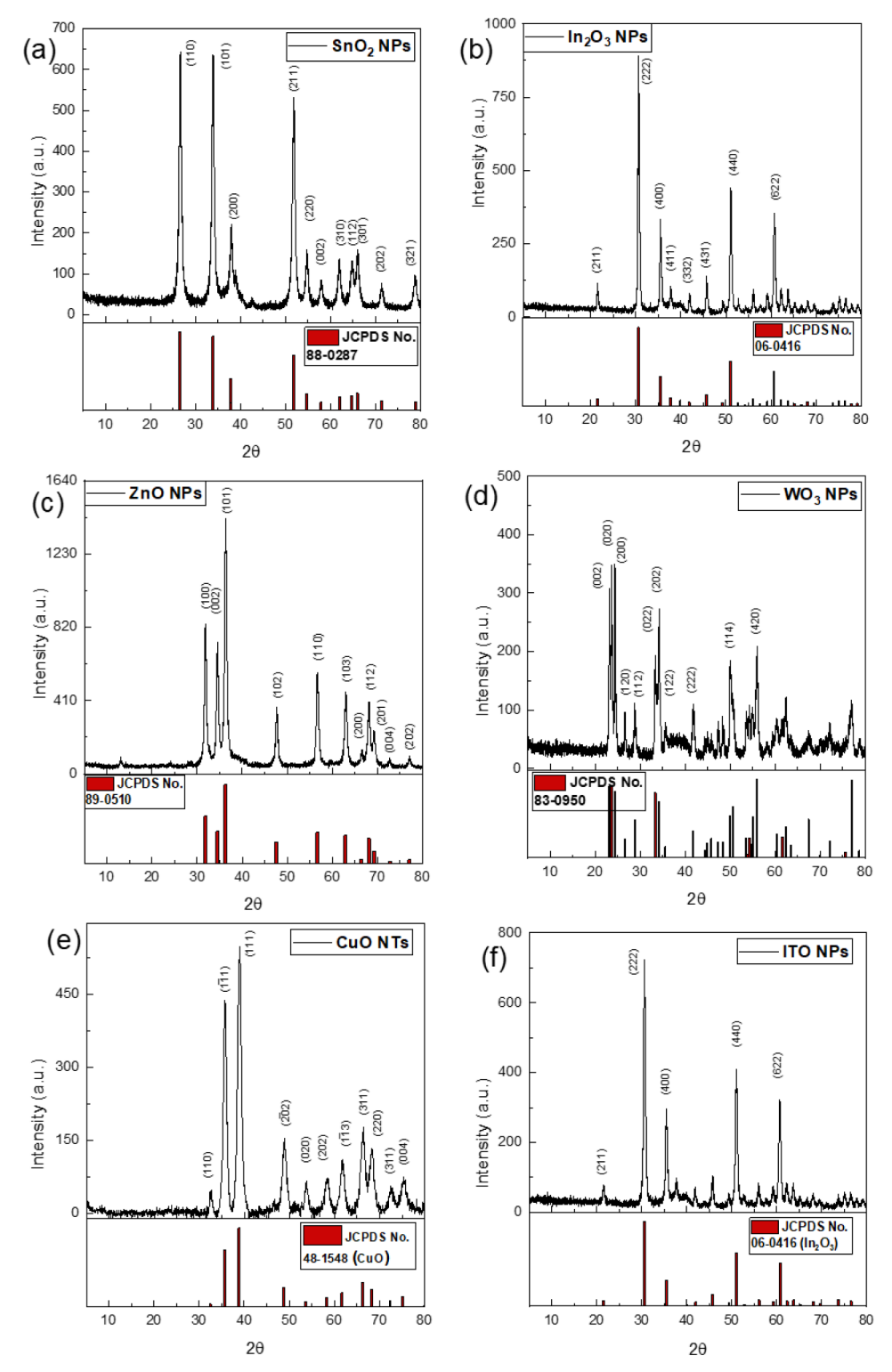


Fig. 2. XRD patterns of (a) SnO₂ NPs, (b) In₂O₃ NPs, (c) ZnO NPs, and (d) WO₃ NPs, (e) CuO NTs, and (f) ITO NPs.

(Fig. 5c). ITO NPs show irregular shape with an average size of 25.9 \pm 13.6 nm (Fig. 5d). Higher magnification analysis shows the lattice planner spacing of $\sim\!2.95$ Å (Fig. 5f) and $\sim\!4.25$ Å (Fig. 5g), corresponding to the (222) and (211) planes of cubic In_2O_3 structure.

Furthermore, UV–Vis diffuse reflection spectra were collected from 200 to1100 nm to determine the band gap energy of the MOS nanostructure using the Tauc method (Eq. (2)) [48,49].

$$\alpha . h v^{\frac{1}{\gamma}} = B \left(h v - E_g \right) \tag{2}$$

Where h = Planck constant, ν = photon's frequency, E_g = estimated band gap energy, and B = constant. γ factor represents the nature of electron transition, which equals 2 and 0.5 for indirect and direct optical transition, respectively. Fig. 6a shows the plotting of $(\alpha h \nu)^2$ vs. $h \nu$ for the direct band gap semiconductors, whereas Fig. 6b shows the plotting of $(\alpha h \nu)^{1/2}$ vs. $h \nu$ for the indirect band gap semiconductors. In these plots, the x-axis intersection point is taken through the extrapolation of the linear portion of the Tauc plot, which gives the estimated band gap

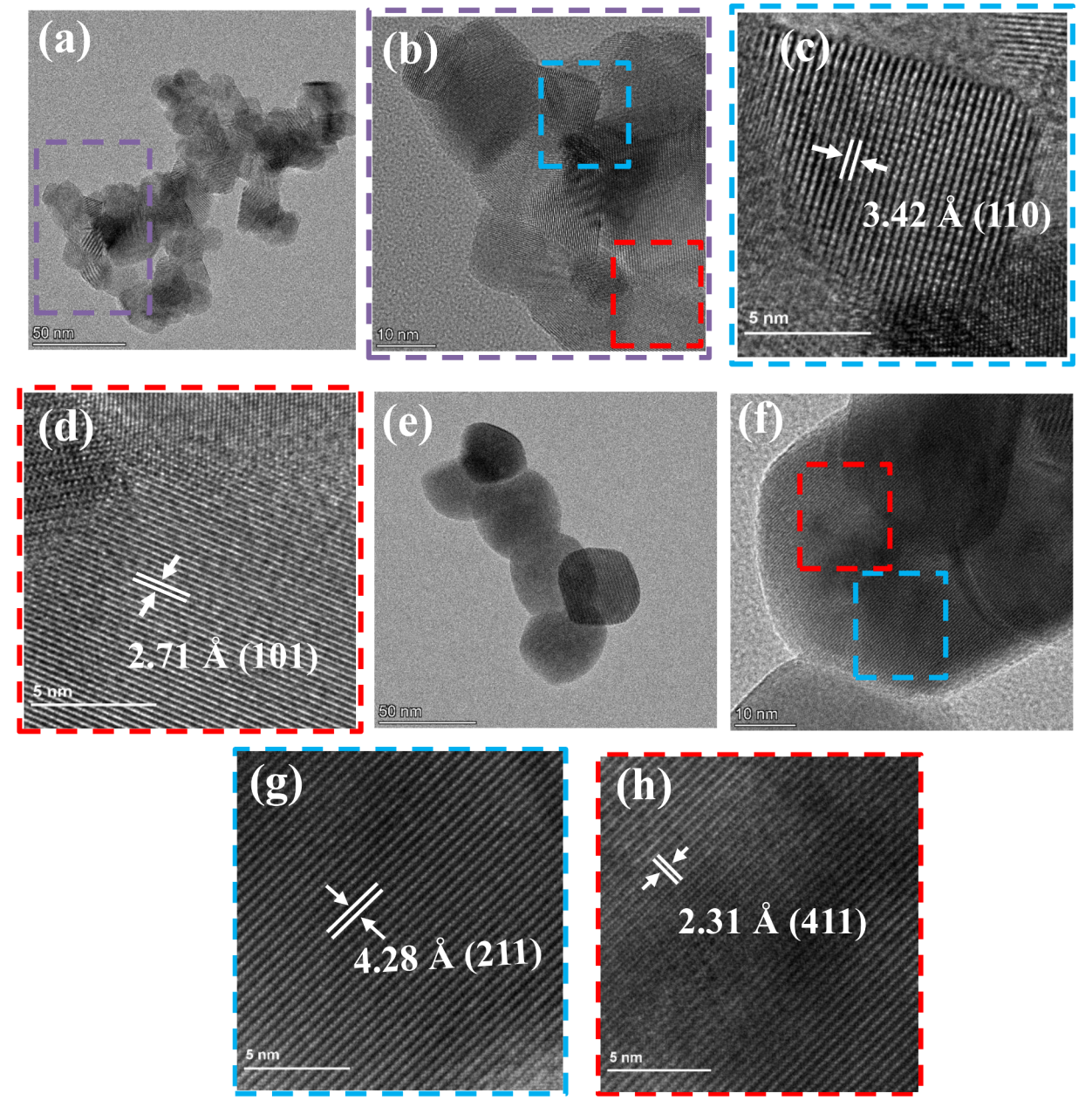


Fig. 3. HR-TEM images of (a,b) SnO₂ NPs and (e,f) In₂O₃ NPs. Magnified lattice fringes and corresponding lattice plane of (c,d) SnO₂ NP and (g,h) In₂O₃ NP.

energy for the MOS nanomaterials (Table 1).

3.2. Light intensity dependent transient optoelectrical response under 400 nm uv illumination

Fig. 7 shows light intensity dependent transient optoelectrical response at room temperature ($21\pm2\,^{\circ}$ C). The optoelectrical response is strongly dependent on the light intensity, where all MOS sensing materials have shown more significant optoelectrical response with an increase in the incident light intensity from 1.1 to 76.0 mW/cm² as shown in Fig. 7a-f. In general, n-type MOS materials show a higher optoelectrical response than p-type MOS materials. Among these n-type MOS materials, direct band gap semiconductor materials demonstrate a higher optoelectrical response (Fig. 7a–c) than indirect band gap semiconductors (Fig. 7d and e). Under the highest optical excitation (i.e., 76.0 mW/cm²), ZnO NPs have exhibited the highest optoelectrical response ($R_p = 1442.4 \pm 149.3$), followed by SnO₂ NPs ($R_p = 500.4 \pm 72.6$), In₂O₃ NPs ($R_p = 20.3 \pm 1.3$). WO₃, an indirect band gap n-type

semiconductor, has shown a R_p of 10.3 ± 2.4 . ITO, a n-type degenerate semiconductor, has indicated a R_p of 7.0 ± 0.6 . CuO, a p-type indirect band gap semiconductor, shows almost no response under light exposure (Fig. 7e). The higher optoelectrical response of direct band-gap semiconductors may be attributed to the direct absorption of photons occurring in these materials compared to indirect band gap semiconductors. As a result, rapid electron transport can occur compared to in-direct band gap semiconductors [55]. Additionally, among the direct band gap materials, SnO2 and ZnO have exhibited higher optoelectrical response, which could be related to their higher surface-to-volume ratio. According to the XRD and HRTEM analysis, SnO2 and ZnO have shown smaller grain sizes (Fig 2a and c) and smaller average NPs size (Figs. 3a and 4a), which might have led to higher light excitation response.

The optoelectrical response also depended on the light intensity (Fig. 7g). Direct band gap n-type semiconductors show higher response with increasing light intensity. Altering light intensity from 1.1 to 76.0 mW/cm², SnO_2 exhibits about 83-fold higher photo response, followed by ZnO (~60-fold) and In_2O_3 (~5-fold). WO_3 , ITO, and CuO

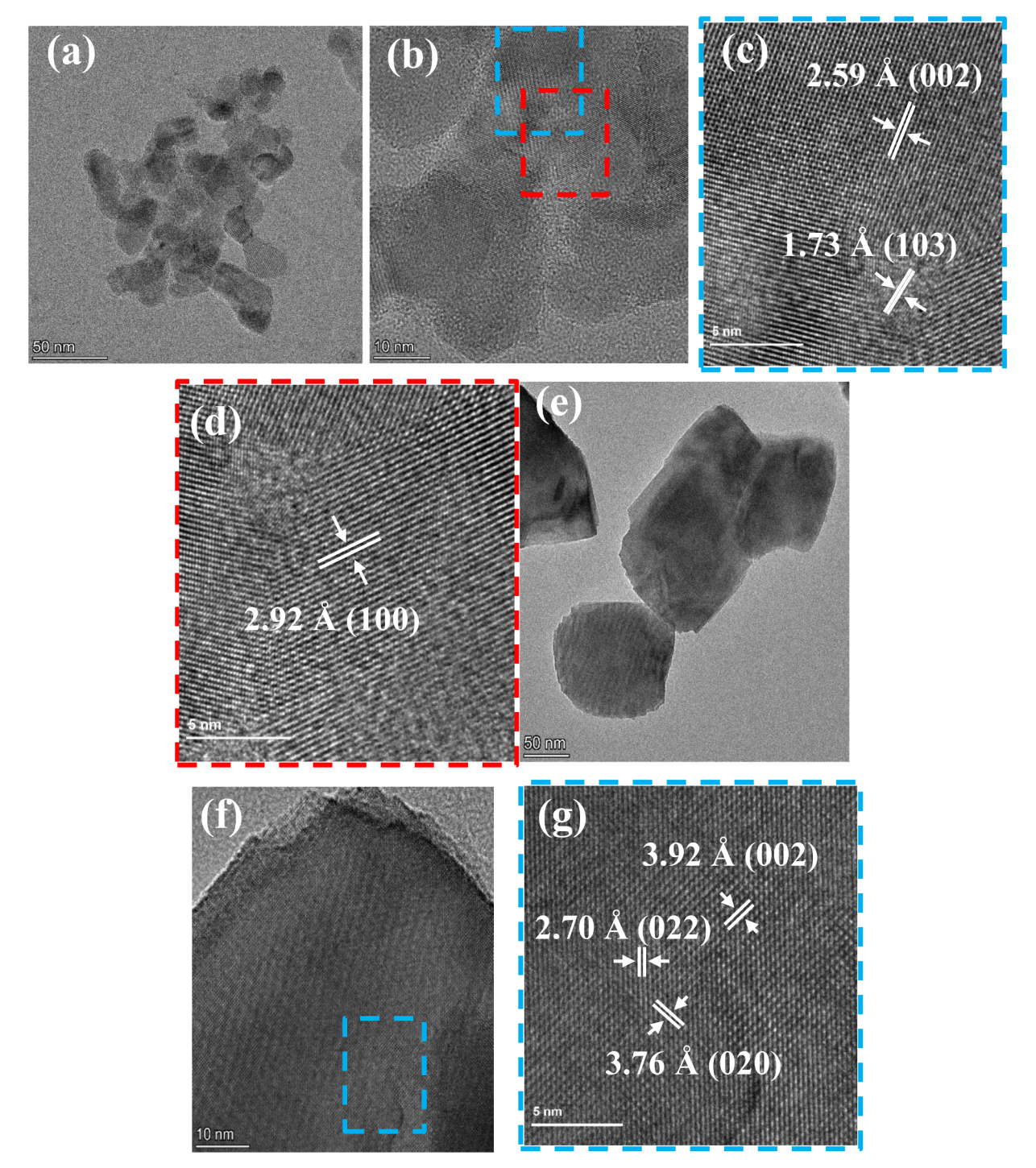


Fig. 4. HR-TEM images of (a,b) ZnO NPs and (e,f) WO₃ NPs. Magnified lattice fringes and corresponding lattice plane of (c,d) ZnO NPs and (g) WO₃ NP.

demonstrate about \sim 4, \sim 4.3, and \sim 1.2-fold enhancement, respectively.

3.3. Optoelectrical response mechanism

Under dark conditions, oxygen molecules from the air capture the free electrons from the MOS conduction band and lower the carrier concentration (Eq. (3)), which leads to higher baseline resistance [56]. As a result, a depletion layer forms near the MOS surface. Under light exposure, the generation of photogenerated electron-hole pairs takes place. Photogenerated holes can move toward the depletion zone and discharge the negatively charged oxygen molecules from the MOS surface (Eq. (4)) [56,57]. In contrast, the photogenerated electrons

accumulated in the MOS conduction band and increased carrier concentration on the MOS surface, which leads to increased MOS conductivity. This is observed in Fig. 7a-f when the baseline resistance reduction has occurred under light exposure. Moreover, the time-dependent optoelectrical response plots were not saturated, possibly due to the presence of sensing materials' surface states [58].

$$O_2(g) + e^- \rightarrow O^{2-}(ads)$$
 (3)

$$h^+ + O^{2-}(ads) \rightarrow O_2(g)$$
 (4)

Additionally, the combination of bulk-related and surface-related processes could explain the overall photoconduction process. When

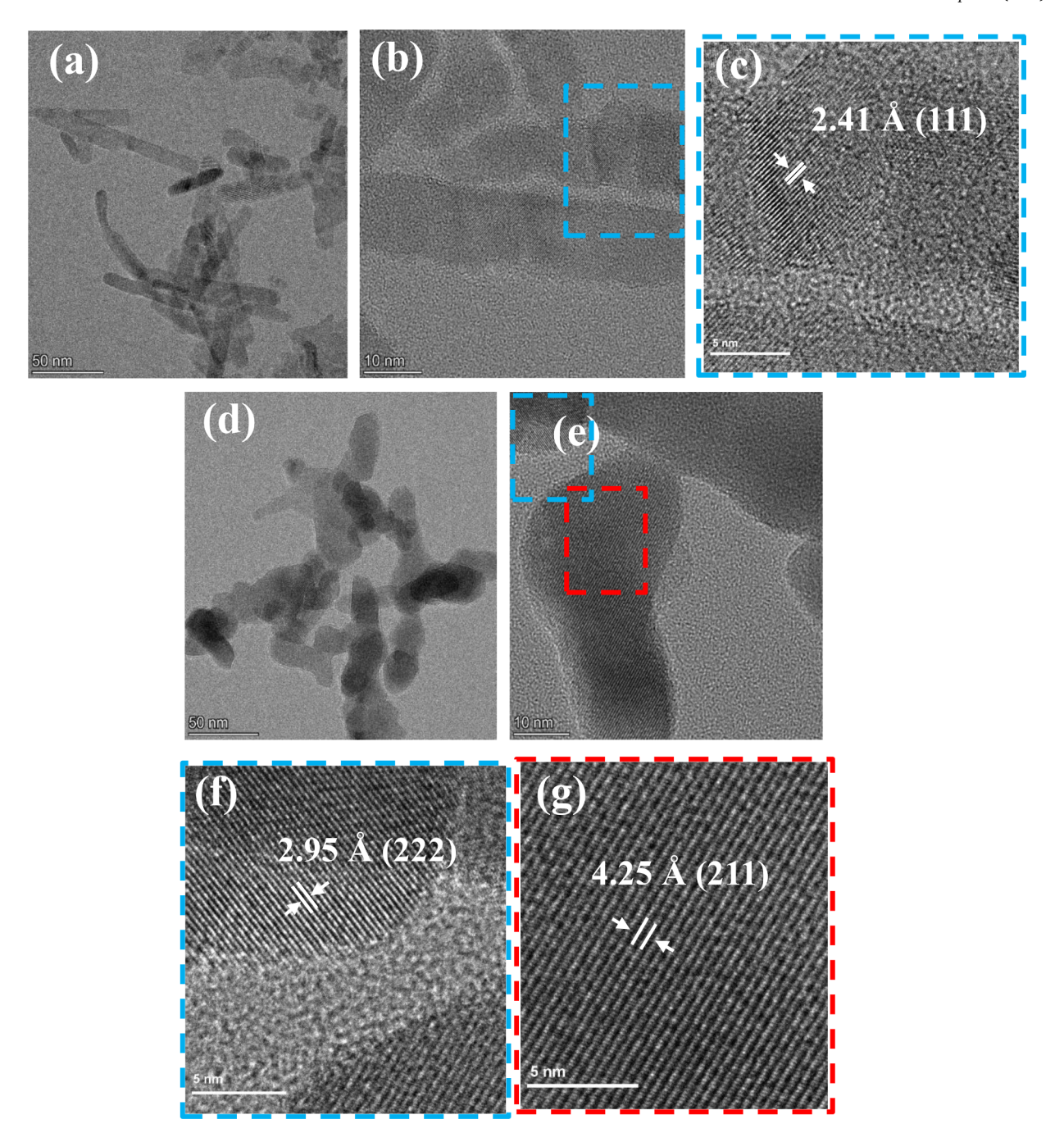


Fig. 5. HR-TEM images of (a, b) CuO NTs and (d, e) ITO NPs. Magnified lattice fringes and corresponding lattice plane of (c) CuO NT and (f, g) ITO NP.

the generation of electron-hole pairs occurs through the photoexcitation of electrons from the valence band to the conduction band, it is known as the bulk-related process [59]. In contrast, the adsorption and desorption of oxygen molecules into defect sites on a material surface is known as the surface-related photoconduction process [59]. Bulk-related processes are faster than surface-related processes [60]. The chemisorption of oxygen occurs at the crystallite's grain boundary under the dark, forming a barrier in the bulk-related process. Upon light excitation, the photoconductivity increases, the height of the barrier reduces, and rapid photo-desorption of oxygen occurs at the grain boundaries [61]. Overall, the chemisorption and photo-desorption process takes place in the bulk of the materials, which leads to a faster response [60,61]. Fig. 7a-f indicates a rapid rise and decay of photoconductance of the MOS materials. Therefore, the photoconduction process could have been majorly dominated by the bulk-related process.

3.4. Gas sensing performance

3.4.1. Sensing performance toward inorganic gases

Real-time sensor responses and normalized sensor responses (S) toward different NO $_2$ concentrations (i.e., 0.05 to 10 ppm $_m$) are shown in Fig. 8a-f and g-l, respectively. ZnO NPs, WO $_3$ NPs, and CuO NTs showed no notable NO $_2$ sensing response under dark conditions, whereas SnO $_2$ NPs, In $_2$ O $_3$ NPs, ITO NPs showed some response with limited recovery. Under 400 nm UV illumination, all MOS sensors show significantly improved NO $_2$ sensing with improved sensor performance (i.e., sensor response, response time, and recovery time). Additionally, stable baseline resistances were observed from all sensors at higher UV illumination (i.e., 36.4 and 76.0 mW/cm 2). Since NO $_2$ is an oxidizing gas, sensor resistance increased for the n-type MOS, whereas the p-type MOS reduced. In general, direct band gap n-type MOS materials show higher

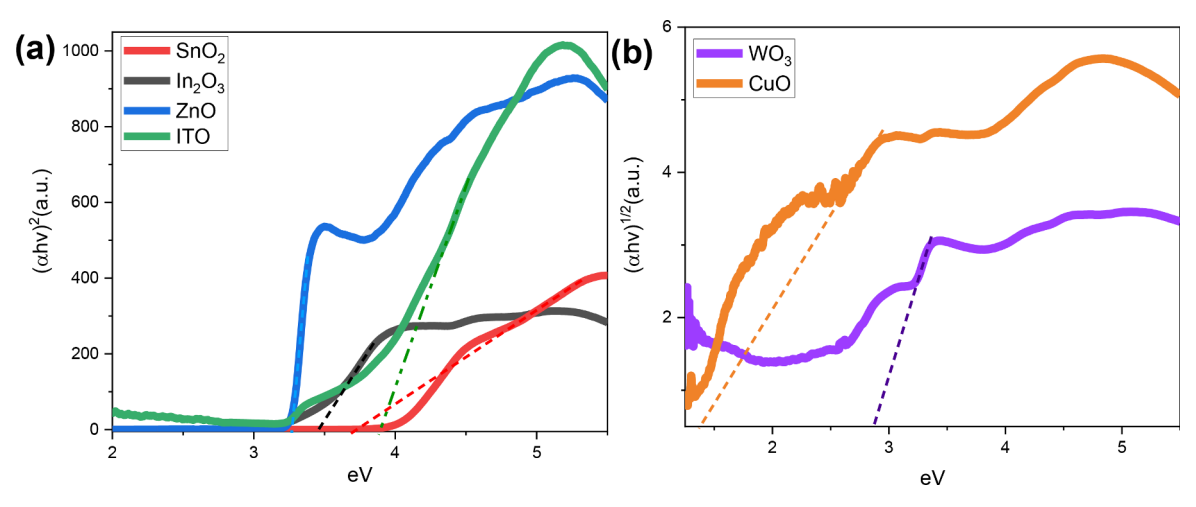


Fig. 6. Tauc's plots for the energy band gap of (a) direct band gap materials, SnO₂ NPs, In₂O₃ NPs, ZnO NPs, and ITO NPs, and (b) indirect band gap materials, WO₃ NPs and CuO NTs.

Table 1
Comparison table of calculated band gap energy of MOS nanomaterials using Tauc's plots in this work and reported in the literature.

MOS Nanomaterials	Band gap energy (eV) (this work)	Band gap energy (eV) (reported in literature)
SnO_2	3.7	-3.70 [50]
In_2O_3	-3.5	3.45 [51]
ZnO	-3.3	-3.23 [52]
WO_3	-2.9	-2.90 [53]
CuO	~1.4	1.20-1.40 [54]
ITO	3.9	3.50-4.30 [43]

NO $_2$ sensor response than indirect band gap n-type semiconductors under UV illumination. Under 76.0 mW/cm $_2$ the highest 10 ppm $_{\rm m}$ NO $_2$ sensing response is observed from SnO $_2$ NPs ($S=\sim$ 470), followed by ZnO NPs ($S=\sim$ 290) > In $_2$ O $_3$ NPs ($S=\sim$ 5.6) > ITO NPs ($S=\sim$ 4.6) > WO $_3$ NPs ($S=\sim$ 2.1). CuO NTs, p-type indirect band gap semiconductor, shows S of 0.23. ITO NPs show lower response than SnO $_2$ NPs and In $_2$ O $_3$ NPs, indicating that degenerate semiconductors respond less to NO $_2$ compared to their pristine counterparts.

Response (T_{s90}) and recovery time (t_{s70}) toward 5 ppm_m NO₂ are shown in (Fig. 8m and n). Under 76.0 mW/cm², CuO NTs shows the best response time ($T_{s90} = \sim 288$ s) followed by SnO₂ NPs ($T_{s90} = \sim 295$ s) <

ITO NPs ($T_{s90} = \sim 407$ s) < $\ln_2 O_3$ NPs ($T_{s90} = \sim 625$ s) < ZnO NPs ($T_{s90} = \sim 662$ s) < WO $_3$ NPs ($T_{s90} = \sim 782$ s). For recovery time, ZnO NPs shows t_{s70} of ~ 71 s < SnO $_2$ NPs ($t_{s70} = \sim 83$ s) < $\ln O_3$ NPs ($t_{s70} = \sim 356$ s) < WO $_3$ NPs ($t_{s70} = \sim 447$ s) ITO NPs ($t_{s70} = \sim 560$ s) < CuO NTs ($t_{s70} = \sim 3443$ s). Although $\ln_2 O_3$ NPs show higher sensing response in the absence of UV light compared to 400 nm UV illumination, the sensor does not recover back to baseline resistance when the sensor is purged with dry air. Ilin et al. also observed a similar result, and the author hypothesized that the NO $_2$ desorption kinetic is slow in the absence of UV light [62].

Additionally, these sensors were tested toward other toxic inorganic gases, including NH $_3$, H $_2$ S, CO, and SO $_2$ under 400 nm UV illumination at room temperature. As shown in Fig. S1, SnO $_2$ NPs show an \sim 2.2-fold improved sensing response toward 100 ppm $_m$ NH $_3$, followed by ZnO NPs (\sim 1.3-fold). WO $_3$ NPs and CuO NTs show \sim 1.6 and \sim 1.2-fold improvement, respectively. A lower sensor response toward H $_2$ S gas under UV illumination was also observed from these MOS sensors (Fig. S2). For example, WO $_3$ NPs and In $_2$ O $_3$ NPs show $_3$ O $_4$ respectively, toward 40 ppm $_3$ H $_2$ S. Additionally, MOS sensors show a minimum response to CO (Fig. S4) and SO $_4$ (data not shown).

3.4.2. Sensing performance toward the volatile organic compounds (VOCs) Fig. 9 shows the sensor response toward ethylbenzene under 400 nm UV illumination at room temperature including dark conditions. In the

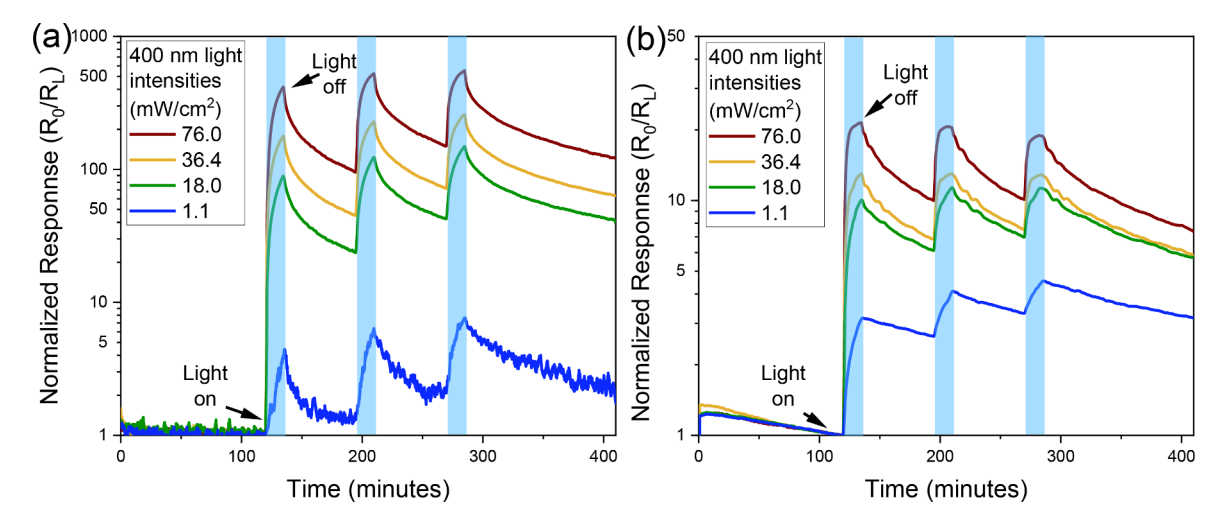


Fig. 7. Transient optical response of (a) SnO_2 , (b) In_2O_3 , (c) ZnO, (d) WO_3 , (e) ZnO, and (f) ITO under 400 nm UV illumination with different light intensity (i.e., 1.1, 18.0, 36.4, 76.0 mW/cm²). R_p (g) and time T_{p90} (h) as a function of light intensity. CuO was marked as X because it does not response to optical excitation.

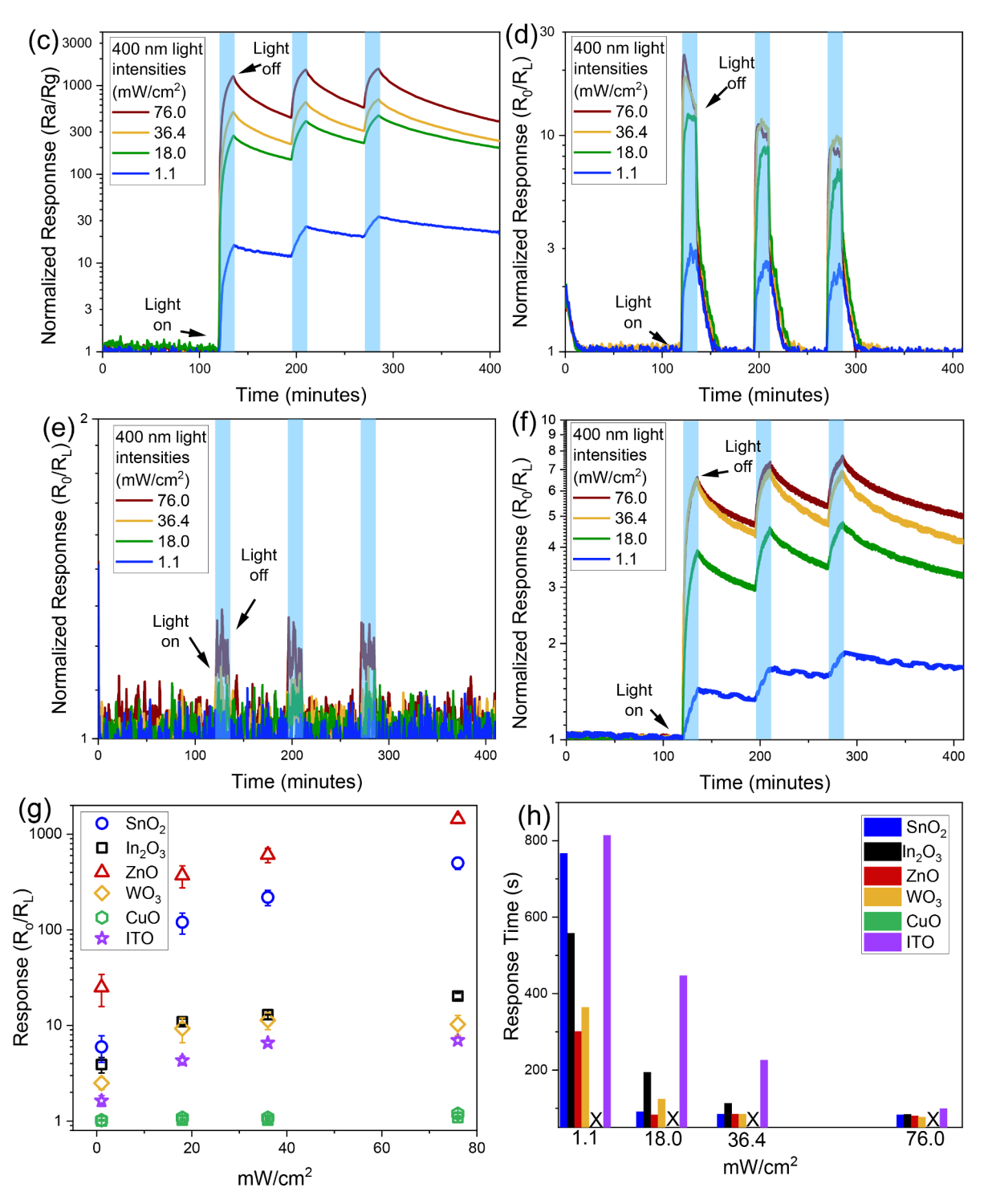


Fig. 7. (continued).

absence of UV illumination, none of the sensors showed any notable response. Upon UV illumination, some of MOS sensors (i.e., WO₃ NPs, SnO₂ NPs, and In₂O₃ NPs) have shown a noticeable improvement in sensor response and faster recovery time, whereas ZnO NPs, CuO NTs, and ITO NPs have demonstrated limited or no effect (Fig. 9a-f). As it relates to WO₃ NPs and In₂O₃ NPs, the optimum ethylbenzene sensing response and response time were observed at 36.4 mW/cm², while SnO₂ NPs shows best sensing performance at 76.0 mW/cm². Changing light intensity from 0.0 to 36.4 mW/cm², WO₃ NPs have shown ~15.4-fold improvement, and In₂O₃ NPs have shown ~2.2-fold improvement in sensing response toward 25 ppm_m ethylbenzene. Calculated T_{s90} for

WO₃ NPs are about 303 s followed by $\rm In_2O_3$ NPs (T_{s90} of 769 s). $\rm SnO_2$ NPs show ~ 3.6 -fold improvement when light intensity increased from 0.0 to 76.0 mW/cm², respectively. $\rm T_{s90}$ for $\rm SnO_2$ NPs is ~ 760 s. The recovery time (t_{S70}) for WO₃ NPs, $\rm In_2O_3$ NPs, and $\rm SnO_2$ NPs are calculated to be 1881s, 3288 s, and 3414 s, respectively, toward 25 ppm_m ethylbenzene for under 76.0 mW/cm².

Similar to ethylbenzene, WO_3 NPs, SnO_2 NPs, and In_2O_3 NPs have improved sensing performance toward p-xylene, whereas ZnO NPs, CuO NTs, and ITO NPs have shown limited or no effect (Fig. S3). These MOS sensors were also tested toward acetone and toluene. No notable sensing response was observed from all MOS sensors in the presence or absence

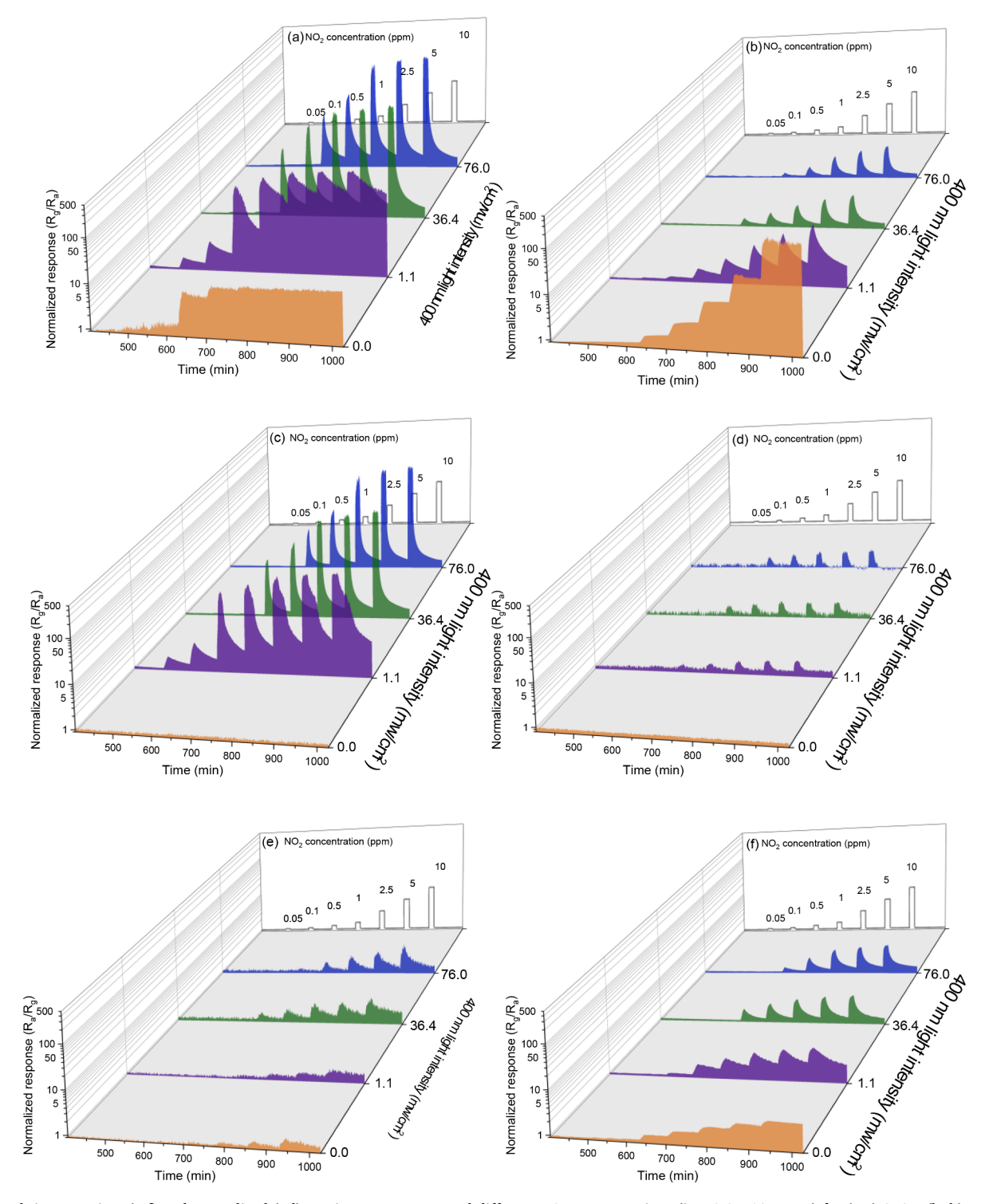


Fig. 8. Real-time transient (a-f) and normalized (g-l) sensing response toward different NO₂ concentrations (i.e., 0.05–10 ppm_m) for (a,g) SnO₂, (b, h) In₂O₃, (c, i) ZnO, (d, j) WO₃, (e, k) CuO, and (f, l) ITO under 400 nm UV illumination with different light intensity (0.0, 1.1, 36.4, 76.0 mW/cm²). 5ppm_m NO₂ response time, T_{s90} , (m) and recovery time, t_{s70} , (n) as a function of light intensity. Symbol X marked no response.

of UV illumination (data not shown).

3.4.3. Sensing mechanisms

According to the ionosorption model, the generation of ionized oxygen species (O_2^- , O^- , O^{2-}) [10,31,63] could differ in MOS-based chemiresistive gas sensors depending on the operating temperature. Oxygen molecules from the air interact with the MOS surface under the

dark, capture electrons from the conduction band, and form O_2^- species at room temperature. Upon light irradiation with enough energy, electron-hole pairs are generated (Eq. (5)) [64]. According to Espid et al., [65] the formation of different atomic oxygen species (O^-, O^{2-}) can also be possible under light illumination (Eqs. 6-9). As a result, a depletion layer forms near the MOS material's surface due to the absorption of oxygen molecules, which leads to an increase in the

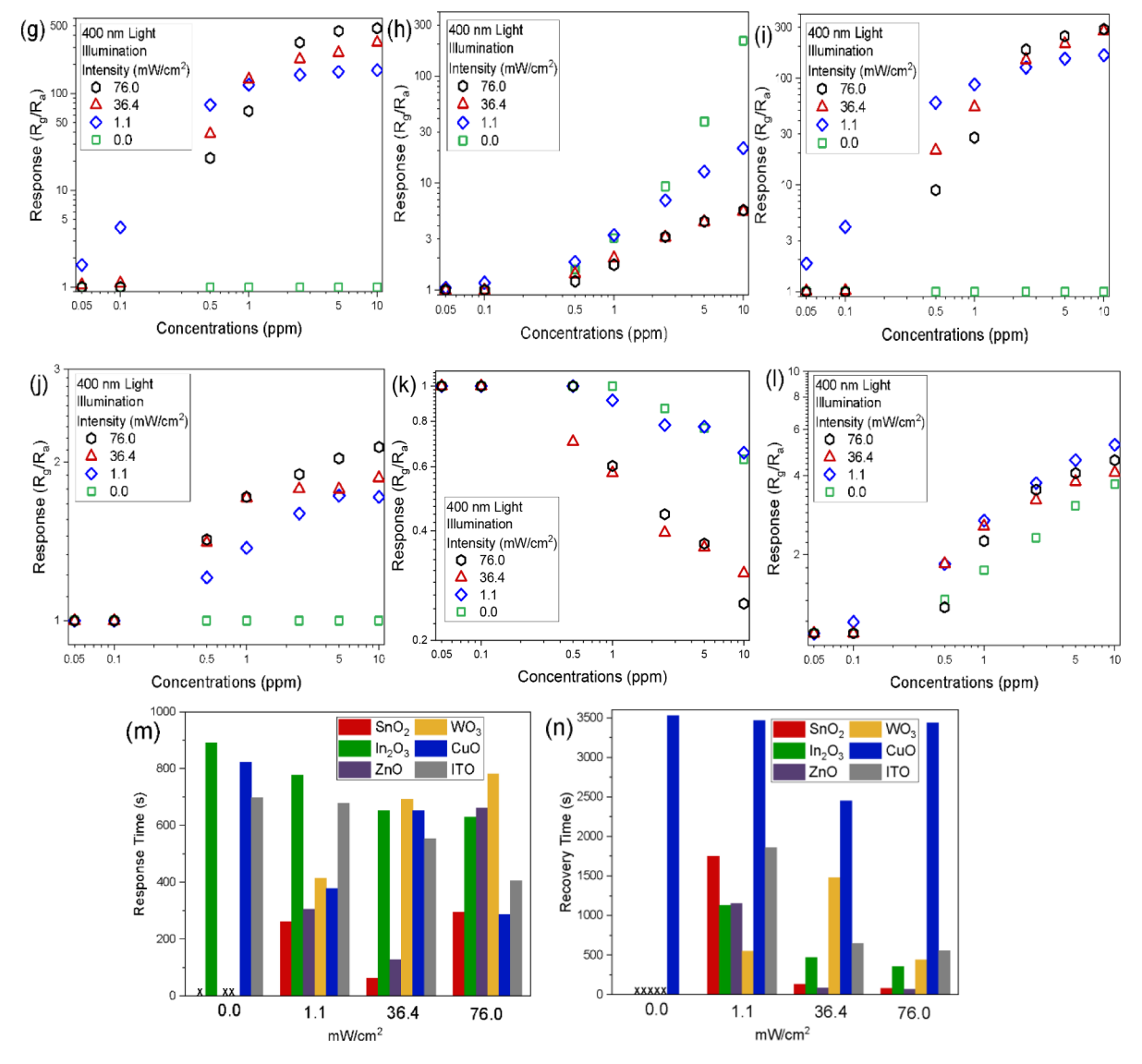


Fig. 8. (continued).

resistance of n-type semiconductor materials. Moreover, optical illumination increases the carrier density in the MOS conduction band and leads to a lower sensor resistance for n-type semiconductors. Additionally, photo-desorption of oxygen species is plausible due to the interaction between the oxygen ions and photo-induced holes; as a result, the resistance of the sensing layer changes over time due to the return of the adsorbed electrons in the conduction band. For example, the resistance decreases for n-type semiconductor materials since electrons are the majority charge carrier (Eq. (9))

$$hv \to h_{(hv)}^+ + e_{(hv)}^-$$
 (5)

$$O_{2(gas)} + e^-_{(hv)} \leftrightarrow O^-_{2(ads)}$$
 (6)

$$O_{2(ads)}^{-} + e_{(hv)}^{-} \leftrightarrow 2O_{(ads)}^{-}$$
 (7)

$$2O_{(ads)}^{-} + e_{(hv)}^{-} \leftrightarrow 2O_{(ads)}^{2-}$$
 (8)

$$O_{2(ads)}^{-} + h_{(hv)}^{+} \leftrightarrow O_{2(gas)}$$
 (9)

Under NO_2 exposure, n-type semiconductors' resistance increased, whereas p-type semiconductors decreased with increasing NO_2 concentrations, as shown in Fig. 5a–f. Ilin et al., [66] state that NO_2

molecules are electron-withdrawing in nature and possess higher electrophilicity (2.30 eV [67]) toward electrons than oxygen molecules (0.44 eV [67]). Therefore, NO₂ could easily bind to the sensing materials' surface and capture the electrons from the conduction band (Eqs. 10 and 11) [66]. As a result, the depletion layer width increased, leading to a higher resistance value in the n-type sensing materials.

$$NO_{2(gas)} \leftrightarrow NO_{2(ads)}$$
 (10)

$$NO_{2(gas)} + e_{(hv)}^{-} \rightarrow NO_{2(ads)}^{-}$$
 (11)

Furthermore, real-time NO_2 sensing data indicated shorter response and recovery time under UV light illumination than dark. The presence of additional photoinduced electrons could have remarkably accelerated the reaction of NO_2 molecules on the MOS surface. Similarly, shorter recovery time could be attributed to the recombination of photoinduced holes and NO_2^- species under light irradiation, which results in a rapid return of trapped electrons to the MOS conduction band [66]. Therefore, the baseline resistance returns to the initial resistance after the NO_2 exposure under light irradiation.

Among all these MOS materials, SnO_2 NPs has shown the highest sensing response toward NO_2 gas under 76 mW/cm². The deeper acceptor level formation on the SnO_2 surface [68] might be a probable

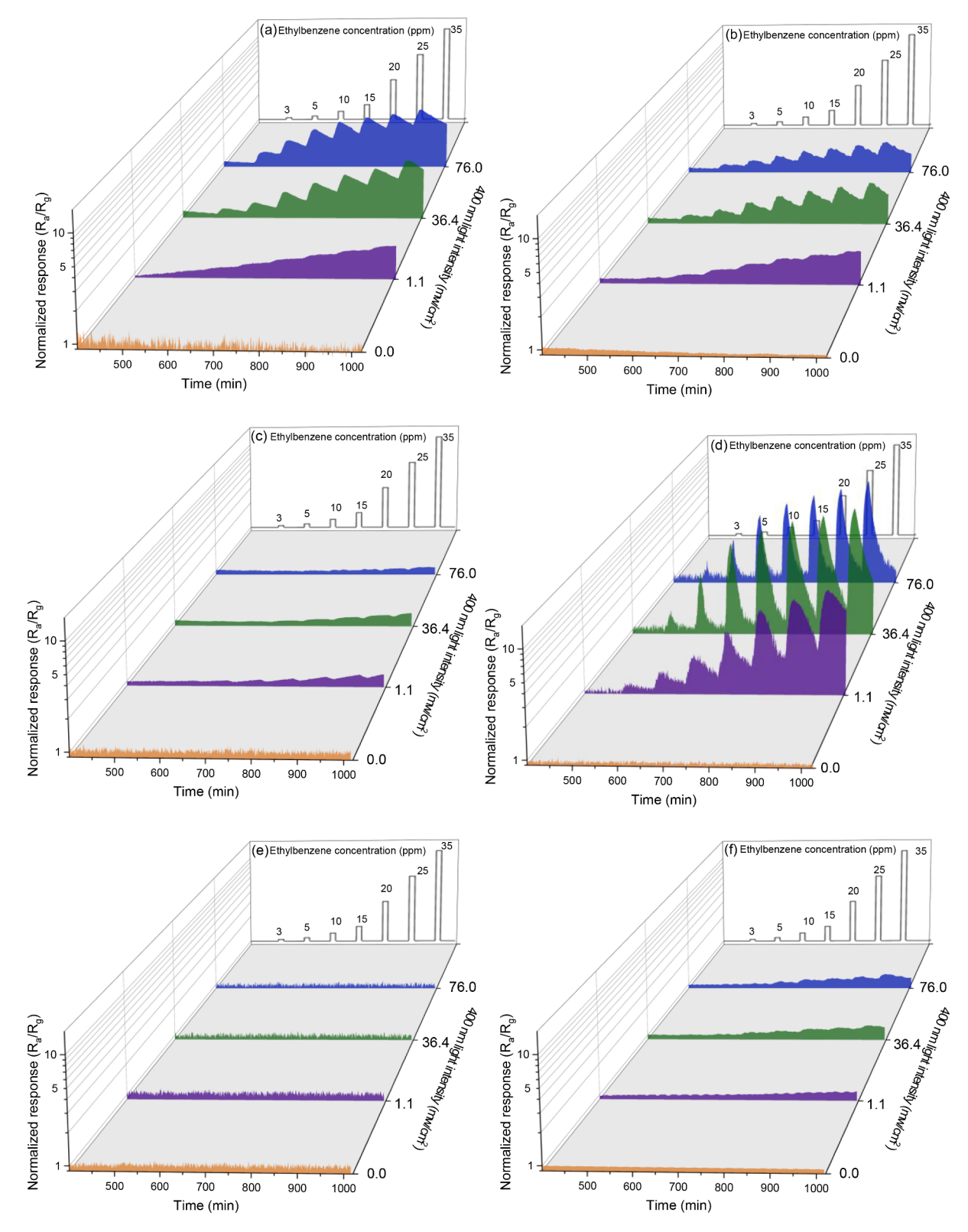


Fig. 9. Real-time transient (a-f) and normalized (g-l) sensing response toward different ethylbenzene concentration (i.e., 3 to $25ppm_m$) for (a, g) SnO_2 , (b, h) In_2O_3 , (c, i) ZnO_3 , (e, i) ZnO_3 , (e, k) ZnO_3 , (e, k) ZnO_3 , (e, k) ZnO_3 , (e, k) ZnO_3 , (f, l) ZnO_3 , (g, k) $ZnO_$

cause for this remarkable NO_2 sensing performance. This phenomenon could have led to the transfer of electrons from the oxygen species to the adsorbed NO_2 molecules, resulting in the formation of a higher number NO_2^- species and a higher sensor resistance. Moreover, SnO_2 NPs consist

of aggregated particles with an average nanoparticle size of 15 nm according to the HRTEM analysis (Fig. 3a). Compared to the other sensing materials employed in this study, $\rm SnO_2$ Nps are relatively small in size, which results in higher specific surface area. As a result, this higher

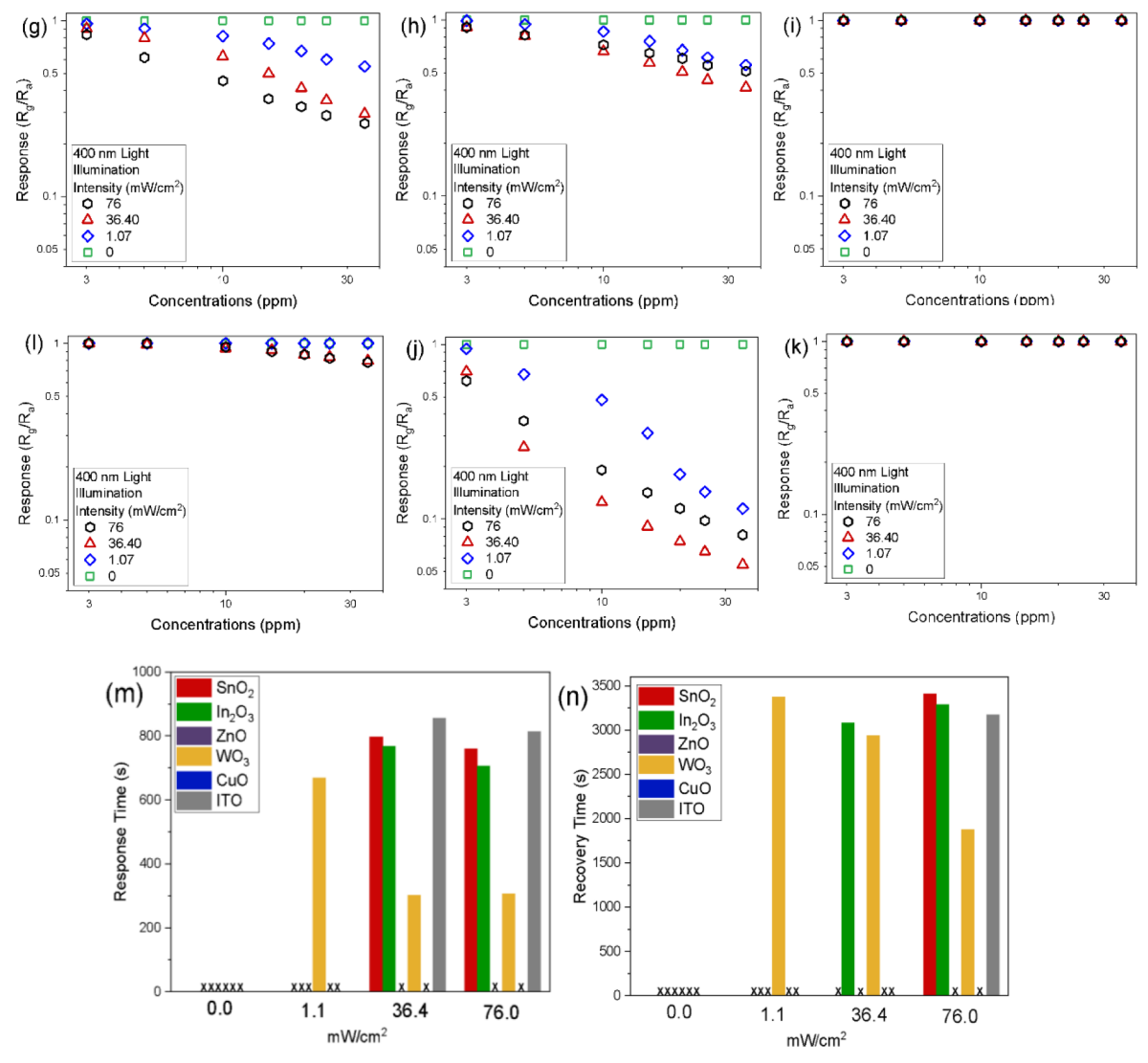


Fig. 9. (continued).

specific surface area could have provided more effective active adsorption sites for NO_2 gas molecules and increased contact interactions between the sensing surface and the analytes. Additionally, the presence of a higher number of photoinduced electron densities under 76.0 mW/cm² could have resulted in the formation of more NO_2^- species and led to an overall better sensing response compared to other MOS sensing materials.

Similarly, a significant sensing performance was observed from n-type MOS semiconductors toward ethylbenzene and p-xylene aromatic compounds at room temperature. The baseline resistance of the sensors decreases upon introducing these aromatic compounds, as shown in Figs. 9a-f and S3. This change in resistance could be attributed to the fact that these aromatic compounds interacted with the adsorbed oxygen species on the MOS surface, formed additional other species in the reaction process, and returned the electron to the conduction band of the MOS. Therefore, we observed the lowering of the baseline resistance. Additionally, these aromatic compounds might not fully dissociate at room temperature and instead could create other more reactive species. Eqs. (12 and 13) show the possible reaction between adsorbed oxygen species and p-xylene [69].

$$C_6H_4(CH_3)_{2(g)} + 2O^-_{(ads)} \rightarrow C_6H_4CH_3CHO_{(ads)} + H_2O_{(g)} + 2e^-$$
 (12)

$$C_6H_4CH_3CHO_{(ads)} + 19O_{(ads)}^- \rightarrow 8CO_{2(g)} + 4H_2O_{(g)} + 19e^-$$
 (13)

Moreover, WO₃ NPs show higher sensitivity toward ethylbenzene and pxylene than SnO₂ NPs, In₂O₃ NPs, ZnO NPs, and ITO NPs. The optimum sensing performance was observed at 36.4 mW/cm². Based on this limited study, increased displacements and reactions of adsorbed oxygen species on the WO3 surface could have led to higher sensing performance. Furthermore, it could have been attributed to employing a specific light wavelength, which improved the photochemical activity between the WO₃ surface and aromatic molecules. According to Gong et al., irradiation wavelength plays an important role in detecting organic compounds [70]. In his work, upon changing the light wavelength from 365 nm to 254 nm, ZnO exhibited significant enhancement in the detection of benzene and toluene, which might be due to the increase in photochemical activity [70]. Additionally, these VOCs possess a highly mobile character, leading to better diffusion ability and further possible reformation into more reactive species by fractional oxidation. This process could undergo additional chemical reactions to fully oxidize on the WO₃ surface, resulting in more electrons being returned to the WO₃ conduction band (Eq. (13)).

3.5. Conclusions

Different n-type (i.e., SnO_2 NPs, In_2O_3 NPs, ZnO NPs, WO $_3$ NPs, ITO NPs) and p-type (i.e., CuO NTs) metal oxide semiconductors were tested

toward several toxic chemicals at room temperature under different 400 nm UV illumination. These materials' electrical and gas sensing properties were systematically analyzed under 400 nm UV illumination with different light intensities (i.e., 0.0-76.0 mW/cm²). A direct correlation was observed between the optoelectrical and NO2 sensing responses. SnO2 NPs showed the highest improvement in sensor response toward NO₂ (~2.7-fold) and optical response (~83-fold) with an increase in UV light intensity from 1.1 to 76.0 mW/cm². In general, higher NO₂ sensing performance was observed from direct band gap n-type MOS than indirect band gap or degenerated n-type MOS. Unlike NO2, indirect band gap n-type WO3 NPs showed the best sensing performance of ethylbenzene and p-xylene with an optimum light intensity at 36.4 mW/cm². This work path is a way for research to develop room-temperature MOSbased chemiresistive gas sensors where the sensing performance can be optimized by adjusting the sensing materials and tuning the optical excitation.

CRediT authorship contribution statement

Suporna Paul: Writing – original draft, Investigation, Data curation. Emily Resendiz Mendoza: Software, Data curation. Dung Thi Hanh To: Writing – review & editing, Visualization, Validation. Thomas F. Stahovich: Visualization, Software, Resources, Methodology, Formal analysis. Jennifer Schaefer: Supervision. Nosang V. Myung: Writing – review & editing, Supervision, Funding acquisition, Conceptualization.

Declaration of competing interest

The authors declare that they have no known competing financial interests or personal relationships that could have appeared to influence the work reported in this paper.

Data availability

Data will be made available on request.

Acknowledgments

This work was partially supported by NSF Convergence Accelerator (NSF ITE-2344028).

Supplementary materials

Supplementary material associated with this article can be found, in the online version, at doi:10.1016/j.snr.2024.100194.

References

- K.L. Morulane, H.C. Swart, D.E. Motaung, A Review on topical advancement and challenges of indium oxide based gas sensors: future outlooks, J. Environ. Chem. Eng. (2024) 112144, https://doi.org/10.1016/j.jece.2024.112144.
- [2] P.O. Ukaogo, U. Ewuzie, C.V. Onwuka, Environmental pollution: causes, effects, and the remedies, Microorgan. Sustain. Environ. Health (2020) 419–429, https://doi.org/10.1016/B978-0-12-819001-2.00021-8.
- [3] P. Berwal, S. Sihag, S. Rani, A. Kumar, A. Jatrana, P. Singh, R. Dahiya, A. Kumar, A. Dhillon, A. Sanger, M. Kumar, A. Sharma, V. Kumar, Hybrid metal oxide nanocomposites for gas-sensing applications: a review, Ind. Eng. Chem. Res. 62 (2023) 14835–14852, https://doi.org/10.1021/acs.iecr.3c02288.
- [4] R.J. Rath, S. Farajikhah, F. Oveissi, F. Dehghani, S. Naficy, Chemiresistive sensor arrays for gas/volatile organic compounds monitoring: a review, Adv. Eng. Mater. 25 (2023) 2200830, https://doi.org/10.1002/adem.202200830.
- [5] J. Yan, Y. Wang, C. Yang, H. Deng, N. Hu, MoS₂/MoO₃ heterojunctions enabled by surface oxidization of MoS₂ nanosheets for high-performance room-temperature NO₂ gas sensing, J. Alloys Compd. 976 (2024) 173208, https://doi.org/10.1016/j. iallcom.2023.173208.
- [6] H.-J. Hu, D.-F. Fan, Z.-H. Ye, Q. Sun, Effects of hyperbaric oxygen on Notch signaling pathway after severe carbon monoxide poisoning in mice, Med. Gas Res. 13 (2022) 23–28, https://doi.org/10.4103/2045-9912.344971.
- [7] R.E. Rodríguez-Martínez, M.Á. Gómez Reali, E.G. Torres-Conde, M.N. Bates, Temporal and spatial variation in hydrogen sulfide (H₂S) emissions during

- holopelagic *Sargassum* spp. decomposition on beaches, Environ. Res. 247 (2024) 118235, https://doi.org/10.1016/j.envres.2024.118235.
- [8] Z. Zhao, L. Zhang, H. Zhang, W. Xin, X. Wang, C. Liu, Y. Guo, Y. Zhuang, W. Jiao, Preparation of La₂O₃/ZnO dodecahedral nanopowders induced by ZIF-8 via an innovative mild aqueous solvent approach and evaluation of their gas-sensitive properties towards H₂S, Mater. Res. Bull. 169 (2024) 112544, https://doi.org/ 10.1016/j.materresbull.2023.112544.
- [9] W. Wang, J. Shen, Y. Chen, D. Zheng, L. Li, Identification and analysis of volatile organic compound and very volatile organic compound of MDF coated with different lacquers and their health risks to humans, J. Environ. Chem. Eng. 12 (2024) 112120. https://doi.org/10.1016/j.jece.2024.112120.
- [10] Z. Li, H. Li, Z. Wu, M. Wang, J. Luo, H. Torun, P. Hu, C. Yang, M. Grundmann, X. Liu, Y. Fu, Advances in designs and mechanisms of semiconducting metal oxide nanostructures for high-precision gas sensors operated at room temperature, Mater. Horiz. 6 (2019) 470–506, https://doi.org/10.1039/C8MH01365A.
- [11] M.R. Alenezi, T.H. Alzanki, A.M. Almeshal, A.S. Alshammari, M.J. Beliatis, S. J. Henley, S.R.P. Silva, A model for the impact of the nanostructure size on its gas sensing properties, RSC Adv. 5 (2015) 103195–103202, https://doi.org/10.1039/C5R419404K
- [12] P. Rai, S.M. Majhi, Y.-T. Yu, J.-H. Lee, Noble metal@metal oxide semiconductor core@shell nano-architectures as a new platform for gas sensor applications, RSC Adv. 5 (2015) 76229–76248, https://doi.org/10.1039/C5RA14322E.
- [13] V.B. Kamble, A.M. Umarji, Gas sensing response analysis of p-type porous chromium oxide thin films, J. Mater. Chem. C. 1 (2013) 8167–8176, https://doi. org/10.1039/C3TC31830C
- [14] S.-W. Chiu, K.-T. Tang, Towards a Chemiresistive sensor-integrated electronic nose: a review, Sens 13 (2013) 14214–14247, https://doi.org/10.3390/s131014214.
- [15] J. Zhang, Z. Qin, D. Zeng, C. Xie, Metal-oxide-semiconductor based gas sensors: screening, preparation, and integration, Phys. Chem. Chem. Phys. 19 (2017) 6313–6329, https://doi.org/10.1039/C6CP07799D.
- [16] H. Nazemi, A. Joseph, J. Park, A. Emadi, Advanced micro- and nano-gas sensor technology: a review, Sens 19 (2019) 1285, https://doi.org/10.3390/s19061285.
- [17] P. Srinivasan, M. Ezhilan, A.J. Kulandaisamy, K.J. Babu, J.B.B. Rayappan, Room temperature chemiresistive gas sensors: challenges and strategies—a mini review, J. Mater. Sci.: Mater. Electron. 30 (2019) 15825–15847, https://doi.org/10.1007/ s10854-019-02025-1.
- [18] J. Spannhake, A. Helwig, O. Schulz, G. Müller, Micro-fabrication of gas sensors, in: E. Comini, G. Faglia, G. Sberveglieri (Eds.), Solid State Gas Sensing, Springer Boston, 2009, pp. 1–46.
- [19] S.E. Zohora, A.M. Khan, N. Hundewale, Chemical sensors employed in electronic noses: a review, in: N. Meghanathan, D. Nagamalai, N. Chaki (Eds.), Advances in Computing and Information Technology, Springer, Berlin, 2013, pp. 177–184.
- [20] S. Gupta Chatterjee, S. Chatterjee, A.K. Ray, A.K. Chakraborty, Graphene-metal oxide nanohybrids for toxic gas sensor: a review, Sens. Actuat. B Chem. 221 (2015) 1170–1181, https://doi.org/10.1016/j.snb.2015.07.070.
- [21] Z. Bo, X. Wei, X. Guo, H. Yang, S. Mao, J. Yan, K. Cen, SnO₂ nanoparticles incorporated CuO nanopetals on graphene for high-performance room-temperature NO₂ sensor, Chem. Phys. Lett. 750 (2020) 137485, https://doi.org/10.1016/j. cplett.2020.137485.
- [22] X. Su, G. Duan, Z. Xu, F. Zhou, W. Cai, Structure and thickness-dependent gas sensing responses to NO₂ under UV irradiation for the multilayered ZnO micro/ nanostructured porous thin films, J. Colloid Interface Sci. 503 (2017) 150–158, https://doi.org/10.1016/j.jcis.2017.04.055.
- [23] J.D. Prades, R. Jimenez-Diaz, F. Hernandez-Ramirez, S. Barth, A. Cirera, A. Romano-Rodriguez, S. Mathur, J.R. Morante, Equivalence between thermal and room temperature UV light-modulated responses of gas sensors based on individual SnO₂ nanowires, Sens. Actuat. B: Chem. 140 (2009) 337–341, https://doi.org/ 10.1016/j.snb.2009.04.070.
- [24] T. Wagner, C.-D. Kohl, C. Malagù, N. Donato, M. Latino, G. Neri, M. Tiemann, UV light-enhanced NO₂ sensing by mesoporous In₂O₃: interpretation of results by a new sensing model, Sens. Actuat. B Chem. 187 (2013) 488–494, https://doi.org/10.1016/j.snb.2013.02.025.
- [25] N.D. Chinh, N.D. Quang, H. Lee, T. Thi Hien, N.M. Hieu, D. Kim, C. Kim, D. Kim, NO gas sensing kinetics at room temperature under UV light irradiation of In₂O₃ nanostructures, Sci. Rep. 6 (2016) 35066, https://doi.org/10.1038/srep35066.
- [26] E. Comini, G. Faglia, G. Sberveglieri, UV light activation of tin oxide thin films for NO₂ sensing at low temperatures, Sens. Actuat. B Chem. 78 (2001) 73–77, https://doi.org/10.1016/S0925-4005(01)00796-1.
- [27] Y. Chen, X. Li, X. Li, J. Wang, Z. Tang, UV activated hollow ZnO microspheres for selective ethanol sensors at low temperatures, Sens. Actuat. B Chem. 232 (2016) 158–164, https://doi.org/10.1016/j.snb.2016.03.138.
- [28] M. Karmaoui, A.B. Jorge, P.F. McMillan, A.E. Aliev, R.C. Pullar, J.A. Labrincha, D. M. Tobaldi, One-Step Synthesis, Structure, and Band Gap Properties of SnO₂ Nanoparticles Made by a Low Temperature Nonaqueous Sol–Gel Technique, ACS Omega 3 (2018) 13227–13238, https://doi.org/10.1021/acsomega.8b02122.
- [29] S. Das, V. Jayaraman, SnO₂: a comprehensive review on structures and gas sensors, Prog. Mater. Sci 66 (2014) 112–255, https://doi.org/10.1016/j. pmatsci.2014.06.003.
- [30] V. Shah, J. Bhaliya, G.M. Patel, P. Joshi, Room-temperature chemiresistive gas sensing of SnO₂ Nanowires: a Review, J. Inorg. Organomet. Polym. Mater. 32 (2022) 741–772, https://doi.org/10.1007/s10904-021-02198-5.
- [31] S. Manohar Majhi, S.T. Navale, A. Mirzaei, H. Woo Kim, S. Sub Kim, Strategies to boost chemiresistive sensing performance of In₂O₃-based gas sensors: an overview, Inorg. Chem. Front. (2023), https://doi.org/10.1039/D3QI00099K.
- [32] M. Samadi, M. Zirak, A. Naseri, M. Kheirabadi, M. Ebrahimi, A.Z. Moshfegh, Design and tailoring of one-dimensional ZnO nanomaterials for photocatalytic

- degradation of organic dyes: a review, Res. Chem. Intermed. 45 (2019) 2197–2254, https://doi.org/10.1007/s11164-018-03729-5.
- [33] N.A. Jayah, H. Yahaya, M.R. Mahmood, T. Terasako, K. Yasui, A.M. Hashim, High electron mobility and low carrier concentration of hydrothermally grown ZnO thin films on seeded a-plane sapphire at low temperature, Nanoscale Res. Lett. 10 (2015) 7, https://doi.org/10.1186/s11671-014-0715-0.
- [34] S.-F. Tseng, P.-S. Chen, S.-H. Hsu, W.-T. Hsiao, W.-J. Peng, Investigation of fiber laser-induced porous graphene electrodes in controlled atmospheres for ZnO nanorod-based NO₂ gas sensors, Appl. Surf. Sci. 620 (2023) 156847, https://doi. org/10.1016/j.apsusc.2023.156847.
- [35] S. Agarwal, L.K. Jangir, K.S. Rathore, M. Kumar, K. Awasthi, Morphology-dependent structural and optical properties of ZnO nanostructures, Appl. Phys. A. 125 (2019) 553, https://doi.org/10.1007/s00339-019-2852-x.
- [36] S.G. Leonardi, Two-dimensional zinc oxide nanostructures for gas sensor applications, Chemosensors 5 (2017) 17, https://doi.org/10.3390/ chemosensors5020017
- [37] O. Samuel, M.H.D. Othman, R. Kamaludin, O. Sinsamphanh, H. Abdullah, M. H. Puteh, T.A. Kurniawan, WO₃-based photocatalysts: a review on synthesis, performance enhancement and photocatalytic memory for environmental applications, Ceram. Int. 48 (2022) 5845–5875, https://doi.org/10.1016/j.ceramint.2021.11.158.
- [38] T.G. Novak, J. Kim, P.A. DeSario, S. Jeon, Synthesis and applications of WO₃ nanosheets: the importance of phase, stoichiometry, and aspect ratio, Nanoscale Adv 3 (2021) 5166–5182, https://doi.org/10.1039/D1NA00384D.
- [39] M.H. Oudah, M.H. Hasan, A.N. Abd, Synthesis of copper oxide thin films by electrolysis method based on porous silicon for solar cell applications, IOP Conf. Ser.: Mater. Sci. Eng. 757 (2020) 012051, https://doi.org/10.1088/1757-899X/ 757/1/012051.
- [40] Z. Lv, C. Zhang, Y. Wang, Z. Kang, X. Gao, Y. Guo, Enhanced high-temperature stability of indium tin oxide - Indium oxide thermocouples by two-step annealing, Thin Solid Films 773 (2023) 139780, https://doi.org/10.1016/j.tsf.2023.139780.
- [41] Z. Yu, I.R. Perera, T. Daeneke, S. Makuta, Y. Tachibana, J.J. Jasieniak, A. Mishra, P. Bäuerle, L. Spiccia, U. Bach, Indium tin oxide as a semiconductor material in efficient p-type dye-sensitized solar cells, NPG Asia Mater. 8 (2016), https://doi.org/10.1038/am.2016.89 e305–e305.
- [42] Y. Ren, P. Liu, R. Liu, Y. Wang, Y. Wei, L. Jin, G. Zhao, The key of ITO films with high transparency and conductivity: grain size and surface chemical composition, J. Alloy. Compd. 893 (2022) 162304, https://doi.org/10.1016/j. iallcom.2021.162304
- [43] Y. Xu, G. Wan, L. Ma, Y. Zhang, Y. Su, D. Liu, G. Wang, Indium tin oxide as a dual-band compatible stealth material with low infrared emissivity and strong microwave absorption, J. Mater. Chem. C. 11 (2023) 1754–1763, https://doi.org/10.1039/D2TC04722E.
- [44] S. Paul, E.R. Mendoza, D.T.H. To, T.T. Tran, T. Stahovich, J. Schaefer, N.V. Myung, Room temperature hydrogen sulfide gas detection using copper oxide nanotube/ indium tin oxide nanoparticle heterojunctions, Sens. Actuat. Rep. 7 (2024) 100185, https://doi.org/10.1016/j.snr.2024.100185.
- [45] K. Wongsaprom, R. Bornphotsawatkun, E. Swatsitang, Synthesis and characterization of tin oxide (SnO₂) nanocrystalline powders by a simple modified sol-gel route, Appl. Phys. A. 114 (2014) 373–379, https://doi.org/10.1007/ s00339-013-8197-y.
- [46] H. Ullah, Z.H. Yamani, A. Qurashi, J. Iqbal, K. Safeen, Study of the optical and gas sensing properties of In₂O₃ nanoparticles synthesized by rapid sonochemical method, J. Mater. Sci. Mater. Electron. 31 (2020) 17474–17481, https://doi.org/ 10.1007/s10854-020-04303-9
- [47] T. Khalafi, F. Buazar, K. Ghanemi, Phytosynthesis and enhanced photocatalytic activity of zinc oxide nanoparticles toward organosulfur pollutants, Sci. Rep. 9 (2019) 6866, https://doi.org/10.1038/s41598-019-43368-3.
- [48] F.A. Mir, Transparent wide band gap crystals follow indirect allowed transition and bipolaron hopping mechanism, Result. Phys. 4 (2014) 103–104, https://doi.org/ 10.1016/j.rinp.2014.06.001.
- [49] P. Makuła, M. Pacia, W. Macyk, How To Correctly determine the band gap energy of modified semiconductor photocatalysts based on UV–Vis spectra, J. Phys. Chem. Lett. 9 (2018) 6814–6817, https://doi.org/10.1021/acs.jpclett.8b02892.
- [50] Synthesis of tin oxide nanoparticles using Nelumbo nucifera leaves extract for electrochemical sensing of dopamine, Int. J. Mod. Phy. B 37 (11) (2023) 2350108, https://doi.org/10.1142/S0217979223501084.
- [51] V. Paolucci, J. De Santis, V. Ricci, L. Lozzi, C. Cantalini, 2D Amorphous/crystalline a-In₂O₃/In₂Se₃ nanosheet heterostructures with improved capability for H₂ and

- NO₂ Sensing, ACS Appl. Nano Mater. 6 (2023) 6011–6023, https://doi.org/
- [52] R. Sonkar, N.J. Mondal, B. Boro, M.P. Ghosh, D. Chowdhury, Cu doped ZnO nanoparticles: correlations between tunable optoelectronic, antioxidant and photocatalytic activities, J. Phys. Chem. Solid. 185 (2024) 111715, https://doi.org/10.1016/j.jpcs.2023.111715.
- [53] C. Lu, D. Cao, H. Zhang, L. Gao, W. Shi, F. Guo, Y. Zhou, J. Liu, Boosted tetracycline and Cr(VI) simultaneous cleanup over Z-Scheme WO₃/CoO p-n heterojunction with 0D/3D structure under visible light, Molecules 28 (2023) 4727, https://doi.org/ 10.3390/molecules28124727.
- [54] A. Bassi, K. Qanungo, I. Hasan, A.A. Alshayiqi, A.S. Ababtain, F.A. Alharthi, CuO nanorods immobilized agar-alginate biopolymer: a green functional material for photocatalytic degradation of amaranth dye, Polym. (Basel) 15 (2023) 553, https://doi.org/10.3390/polym15030553.
- [55] M.A. Hadi, M. Nurul Islam, J. Podder, Indirect to direct band gap transition through order to disorder transformation of Cs₂AgBiBr₆ via creating anti-site defects for optoelectronic and photovoltaic applications, RSC Adv. 12 (2022) 15461–15469, https://doi.org/10.1039/D1RA06308A.
- [56] Z.Q. Bai, Z.W. Liu, A broadband photodetector based on Rhodamine B-sensitized ZnO nanowires film, Sci. Rep. 7 (2017) 11384, https://doi.org/10.1038/s41598-017-11154-8
- [57] Y.-L. Chu, S.-J. Young, L.-W. Ji, I.-T. Tang, T.-T. Chu, Fabrication of ultraviolet photodetectors based on Fe-Doped ZnO nanorod structures, Sens 20 (2020) 3861, https://doi.org/10.3390/s20143861.
- [58] S.P. Ghosh, K.C. Das, N. Tripathy, G. Bose, D.H. Kim, T.I. Lee, J.M. Myoung, J. P. Kar, Ultraviolet photodetection characteristics of zinc oxide thin films and nanostructures, IOP Conf. Ser. Mater. Sci. Eng. 115 (2016) 012035, https://doi.org/10.1088/1757-899X/115/1/012035.
- [59] S.K. Mishra, R.K. Srivastava, S.G. Prakash, Photoluminescence and photoconductivity studies of ZnO nanoparticles prepared by solid state reaction method, J. Mater. Sci. Mater. Electron. 24 (2013) 125–134, https://doi.org/ 10.1007/s10854-012-0950-z.
- [60] J.S. Jie, W.J. Zhang, Y. Jiang, X.M. Meng, Y.Q. Li, S.T. Lee, Photoconductive characteristics of single-crystal CdS nanoribbons, Nano Lett. 6 (2006) 1887–1892, https://doi.org/10.1021/nl060867g.
- [61] P. Sharma, K. Sreenivas, K.V. Rao, Analysis of ultraviolet photoconductivity in ZnO films prepared by unbalanced magnetron sputtering, J. Appl. Phys. 93 (2003) 3963–3970, https://doi.org/10.1063/1.1558994.
- [62] A. Ilin, N. Fantina, M. Martyshov, E. Forsh, P. Forsh, P. Kashkarov, in: UV effect on NO₂ sensing properties of nanocrystalline In₂O₃, 3rd International Conference on Nanotechnologies and Biomedical Engineering, Singapore 55, Springer, 2016, pp. 340–344. https://doi.org/10.1007/978-981-287-736-9 82.
- [63] B.M. Babar, S.H. Sutar, S.H. Mujawar, S.S. Patil, U.D. Babar, U.T. Pawar, P. M. Kadam, P.S. Patil, L.D. Kadam, V₂O₅-rGO based chemiresistive gas sensor for NO₂ detection, Mater. Sci. Eng. B. 298 (2023) 116827, https://doi.org/10.1016/j.mseb.2023.116827.
- [64] S.-W. Fan, A.K. Srivastava, V.P. Dravid, UV-activated room-temperature gas sensing mechanism of polycrystalline ZnO, Appl. Phys. Lett. 95 (2009) 142106, https://doi.org/10.1063/1.3243458.
- [65] E. Espid, F. Taghipour, Development of highly sensitive ZnO/In₂O₃ composite gas sensor activated by UV-LED, Sens. Actuat. B Chem. 241 (2017) 828–839, https://doi.org/10.1016/j.snb.2016.10.129.
- [66] A. Ilin, M. Martyshov, E. Forsh, P. Forsh, M. Rumyantseva, A. Abakumov, A. Gaskov, P. Kashkarov, UV effect on NO₂ sensing properties of nanocrystalline In2O3, Sens. Actuat. B Chem. 231 (2016) 491–496, https://doi.org/10.1016/j. snb.2016.03.051.
- [67] H. Bai, H. Guo, C. Feng, J. Wang, B. Liu, Z. Xie, F. Guo, D. Chen, R. Zhang, Y. Zheng, Highly responsive and selective ppb-level NO₂ gas sensor based on porous Pd-functionalized CuO/rGO at room temperature, J. Mater. Chem. C. 10 (2022) 3756–3769, https://doi.org/10.1039/D1TC05231D.
- [68] T. Hyodo, K. Urata, K. Kamada, T. Ueda, Y. Shimizu, Semiconductor-type SnO₂-based NO₂ sensors operated at room temperature under UV-light irradiation, Sens. Actuat. B Chem. 253 (2017) 630–640, https://doi.org/10.1016/j.snb.2017.06.155.
- [69] S. Lu, X. Hu, H. Zheng, J. Qiu, R. Tian, W. Quan, X. Min, P. Ji, Y. Hu, S. Cheng, W. Du, X. Chen, B. Cui, X. Wang, W. Zhang, Highly selective, ppb-level xylene gas detection by Sn²⁺-doped NiO flower-like microspheres prepared by a one-step hydrothermal method, Sens 19 (2019) 2958, https://doi.org/10.3390/s19132958.
- [70] J. Gong, Y. Li, X. Chai, Z. Hu, Y. Deng, UV-light-activated ZnO fibers for organic gas sensing at room temperature, J. Phys. Chem. C. 114 (2010) 1293–1298, https:// doi.org/10.1021/jp906043k.